Journal of Power Sources 220 (2012) 54–64

Contents lists available at SciVerse ScienceDirect

Journal of Power Sources

journal homepage: www.elsevier.com/locate/jpowsour

Investigation of degradation mechanisms of a high-temperature polymer-electrolyte-membrane fuel cell stack by electrochemical impedance spectroscopy

Ji-Rae Kim, Jung S. Yi*, Tae-Won Song

SAIT, Samsung Electronics Co. Ltd., San 14, Nongseo-dong, Giheung-gu, Yongin-si, Gyeonggi-do 446-712, Republic of Korea

HIGHLIGHTS

- A graphical method of analyzing the EIS results of PEM fuel cells is introduced.
- The EIS analysis can identify degradation mechanisms of PEM fuel cell stacks.
- Loss of electrolytes can increase the H^+ transport resistance of cathode electrode.
- The ORR charge transfer resistance can be affected by the O_2 transport rate.
- The transport limiting step of O_2 is through the electrolytes in the catalyst layer.

ARTICLE INFO

Article history:
Received 14 May 2012
Received in revised form
10 July 2012
Accepted 31 July 2012
Available online 9 August 2012

Keywords:
Polymer-electrolyte-membrane fuel cell
Electrochemical impedance spectroscopy
Fuel cell stack
Degradation mechanism
Diagnostics

ABSTRACT

Retaining optimum acid-contents in membranes and electrodes is critical to maintaining the performance and durability of acid-doped high-temperature (HT) polymer-electrolyte-membrane fuel cells (PEMFCs). Since the distribution of acids is influenced by the operating and compression conditions of the stack, there is great demand for understanding the behavior of individual membrane-electrode-assemblies (MEAs) while operating the cells in a stack. In this study, an *in-situ* diagnosis method using electrochemical impedance spectroscopy (EIS) is implemented during the durability test of an HT-PEMFC stack. Adopting a lumped equivalent-circuit model, the specific parameters are obtained from EIS results, and the changes of the values are compared with the performance loss of individual MEA. From this analysis it can be concluded that the main cause of performance degradation of the stack is due to the loss of electrolytes in the cathode, which leads to an increase in the proton transport resistance of cathode catalyst layers. In addition to the proton transport loss in the cathode, the charge transfer resistance of the oxygen reduction reaction has contributed to the performance decay of the stack. The causes of the increase in the cathode charge transfer resistance for each cell of the stack are discussed.

1. Introduction

Polymer-electrolyte-membrane fuel cells (PEMFCs) have distinctive characteristics that are suited for transportation, mobile as well as stationary applications [1]. Since its typical operating temperature is below 100 °C, water management becomes an important issue in order to maintain high proton conductivity of the membrane without causing flooding of the gas diffusion layers (GDLs). In addition, when hydrocarbon fuels are used for the source of the fuel, great consideration has to be taken to minimize the impact of carbon monoxide poisoning. Thus, high-temperature (HT) PEMFCs, which are designed to operation at temperatures above 100 °C without the need for external humidification, are gaining attention, especially when the systems are integrated with fuel-reforming processes [2]. Various attempts have been made to develop a new generation of organic proton conductors, which allow operating at higher temperatures without external humidification [3–12]. Among the various materials developed, the polybenzimidazole (pBI)-based phosphoric-acid doped membrane, which is permitted to work at 150–180 °C, is the only kind that has been proved for commercial use [8]. The durability of the fuel cells, however, is an issue that remains to be addressed, and it is speculated that the acid distribution in the cathode electrode significantly impacts the durability of the cells [12]. This means that the acid distribution of the individual cell in a stack is greatly influenced by the operating and compression conditions of that particular stack.

* Corresponding author. Tel.: +82 31 280 6886; fax: +82 31 280 9359.
E-mail address: jinkyi2000@yahoo.com (J.S. Yi).

0378-7753/$ – see front matter © 2012 Elsevier B.V. All rights reserved.
http://dx.doi.org/10.1016/j.jpowsour.2012.07.129

In this article, electrochemical impedance spectroscopy (EIS) is used as an *in-situ* diagnostic tool to understand the degradation behavior over the long-term operation of an HT-PEMFC stack.

2. Experimental

A six-cell stack was built with home-made membrane-electrode-assemblies (MEAs). Platinum catalysts (Tanaka Metal Co.), where 46.6 wt% of Pt was dispersed on Vulcan carbon, was used as an anode material, and a binary ally system, Pt–Co on Ketjen Black carbon (Tanaka Metal Co., TEC36E52), was used as the cathode catalyst material. The composition of the alloy catalyst was 45.9 wt % of Pt and 5 wt% of Co. The catalyst slurry was composed of the catalyst, Polyvinylidenefluoride (Aldrich) as a binder, and N-methyl-2-pyrrolidone (Aldrich) as a solvent. The slurry was well mixed in its uniform and homogeneous state by Thinky mixer. For both the gas-diffusion-electrodes (GDEs), the catalyst slurry was coated onto the GDL (35BC, SGL carbon), which is made of porous carbon paper, using a wire bar and dried in the oven. The amount of Pt loading was set to 0.9 mg Pt cm^{-2} for the anode and 1.7 mg Pt cm^{-2} for the cathode, respectively. Then, a sheet of membrane, a film of polybenzoxazine (pBOA)-pBI co-polymer, doped in 85 wt% phosphoric acid solution was sandwiched between the anode and cathode GDEs [13]. The size of the active area was 120 cm^2, and graphite-based composite bipolar plates (w/phenolic resins), which have multi-serpentine channels, and 500-μm-thick FKM gaskets, which are placed around the circumference of the active area on both sides of an MEA, were used to build a six-cell assembly of MEAs and bipolar plates. The six-cell assembly was then placed between two sheets of stainless steel endplates to build a stack, and the stack was compressed to 17.7 kN using eight sets of compression springs and tie rods placed around the circumference of the endplates.

Using the heaters imbedded in both endplates, the six-cell stack was heated to 150 °C, while dry hydrogen was fed to the anode at a flow rate equivalent to 0.8H_2 utilization (U_{H2}) at 0.2 A cm^{-2}, and dry air was fed to the cathode at a flow rate equivalent to 0.5 O_2 utilization (U_{O2}) at 0.2 A cm^{-2}. At the exits of the gas streams, a near ambient pressure was maintained for both anode and cathode. Once the stack had reached the desired temperature, a durability test was performed applying a constant current at 0.2 A cm^{-2}. During the durability testing, EIS measurements were taken at the same current density using Solarton impedance spectroscopy (Solatron SI 1287 Electrochemical Interface) and Solatron impedance analyzer (Solatron SI 1260 Impedance/Gain-Phase Analyzer). The wires of the working and the counter electrodes were connected to both the current collectors placed at the end of the stack between the bipolar plate and the endplate, and the sensing and the reference electrodes were connected at the edge of the bipolar plates placed around the measuring MEA. The measurements were taken for every cell in the stack starting from the cathode-end MEA to the anode-end MEA of the stack. During the measurements, 10 mV of voltage perturbation was applied by sweeping the frequency from 10 kHz to 0.05 Hz with 10 points per decade interval.

After 4000 h of durability testing the stack was disassembled and the acid-base titration was performed for the individual MEA. From each side of the MEA, both anode and cathode GDEs were peeled off from the membrane, and five pieces of 1-cm-diameter circles, which are taken at the center and equally spaced along the cathode flow path, were taken from each piece of both anode and cathode GDEs and the membrane. Using a Metrohm 798 MPT titrino, the acid-base titration was conducted to estimate the amount of acid remaining in the GDEs and the membrane of each MEA. The detailed procedure of the acid-base titration can be found in Ref. [12].

3. Results and discussion

3.1. Voltage degradation of the stack during the constant-current durability test

The durability test results of the stack tested at 0.2 A cm^{-2} for 4000 h of continuous operation are depicted in Fig. 1. The voltage of individual MEA is monitored and plotted. The initial average voltage of the six-cell stack is 0.590 V, and the voltage has increased to 0.688 V on an average over 560 h of the operation. The peak voltage of the individual MEA varies within 15 mV among the cells. The causes of the performance differences are expected mainly due to the variability of MEA properties, and they may also be attributed to the temperature distribution within the stack. Once each MEA reaches the peak performance, the voltages of all the MEAs are decreased monotonously up to about 2000 h with an average decay rate of 15.6 ± 3.8 μv h^{-1}. The range of the first decay period varies between 1800 and 2500 h. In general, the MEAs having higher peak voltages keep the first decay period longer than the ones having lower values. From the end of the first decay period, a noticeable change in the decay rate is observed, showing 52.7 ± 9.1 μV h^{-1} on an average until the testing is terminated at almost 4000 h. This period is called the *second decay period* as depicted in Fig. 1. At the end of the test, the average final voltage of the stack is reached at 0.582 V; however, more than 60 mV differences between the best and the worst performing MEAs are observed.

The observed decay rate of the stack is noticeably higher than the typical values reported for HT-PEMFCs [14]. To mitigate the causes of the high-rate decay of the stack performance, understanding of the degradation mechanisms is critical with demanding for *in-situ* diagnostic methodologies that can be implemented to the individual cell in the stack without interrupting the long-term durability testing of the stack.

3.2. EIS analysis method

To investigate the performance degradation mechanisms during the second decay period, EIS measurements are taken for the individual MEA at 1800, 2200, 2800, and 3300 h. In addition to the change in individual cell voltage over time shown in Fig. 1, the EIS measurements can provide additional information on the cell by taking the response of voltage change as an oscillating current density or vice versa. The results provide the information related to

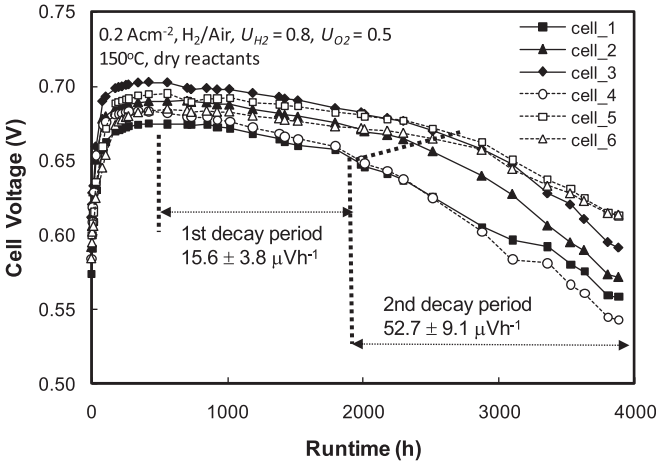

Fig. 1. Results of a constant-current durability test of a six-cell HT-PEMFC stack. The stack is maintained at 0.2 A cm^{-2} and 150 °C while supplying dry hydrogen ($U_{H2} = 0.8$) and dry air ($U_{O2} = 0.5$) at near-ambient pressure.

the changes of the kinetics and the transport processes with regard to electrochemical reaction rates at different ranges of frequencies of oscillation. The results of the impedance spectroscopy are typically expressed as Nyquist or Bode plots, as shown in Figs. 2 and 3, respectively. For all the cases investigated, two arcs that have shifted away from the origin are observed as depicted in Fig. 2.

During the measurement the protons are conducted through the membrane and the electrons are transported through the solid conducting layers, including GDLs and bipolar plates for both anode and cathode. Both the proton conducting membrane and the electron conducting layers behave similar to the resistors connected in a series, and the equivalent magnitude of the resistance of the sum of the proton conducting membrane and the electron transporting solid layers is called the *ohmic resistance* (R_{ohmic}) and can be obtained by taking the magnitude of the real part of impedance at the high-frequency region where the value of the imaginary part of impedance is zero. It is well accepted that the intercept of the real axis at high frequencies near 1 kHz corresponds to the ohmic resistance for PEMFCs. In these measurements, the ohmic resistances are obtained between 0.8 and 6.3 kHz.

Near the high-frequency region the signature of anode impedance may also appear. In this study, the effect of anode impedance is ignored based on an assumption that the contribution of anode impedance is insignificant compared with the contribution of the cathode electrode, which is supported by the comparison of EIS results between the normal fuel cell mode and the hydrogen-pump mode where hydrogen is fed on both sides of the electrode. The results of the comparison are not included in this article; however, more discussion related to the anode impedance can be found in Ref. [12].

When the contribution of anode impedance is ignored, the first arc shown in Fig. 2 represents the contribution of the cathode electrode for the charge transfer rate of the oxygen reduction reaction (ORR). By considering only the forward reaction for a modified Butler–Volmer equation, the kinetic expression of the ORR can be expressed as given next:

$$i = i_0 \cdot A_{\text{pt}} \cdot \left(\frac{C_{\text{O2}}}{C^*_{\text{O2}}}\right) \exp\left(\frac{4\alpha \cdot F}{R \cdot T}\eta_{\text{ORR}}\right) \quad (1)$$

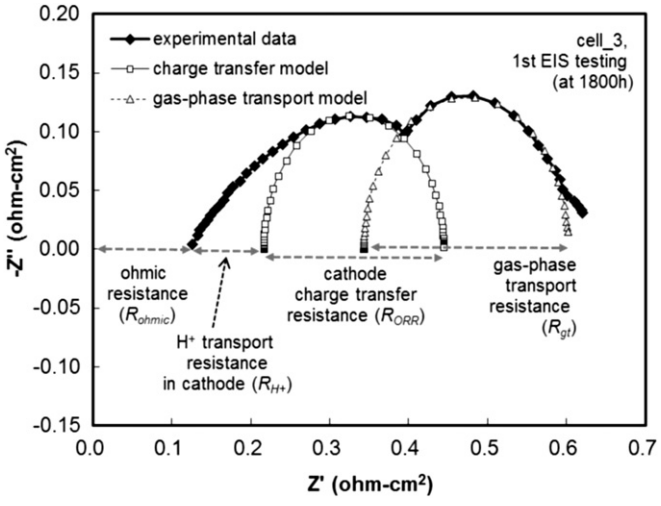

Fig. 2. A Nyquist plot of a cell measured during the constant-current durability test of the HT-PEMFC stack. The graphical methods used in estimating each resistance are plotted over the experimental data. During the testing the stack is maintained at 0.2 A cm^{-2} and 150 °C by supplying dry hydrogen ($U_{\text{H2}} = 0.8$) and dry air ($U_{\text{O2}} = 0.5$) at near-ambient pressure, and the 10 mV voltage perturbation is applied sweeping the frequency from 10 kHz to 0.05 Hz with 10 points per decade interval.

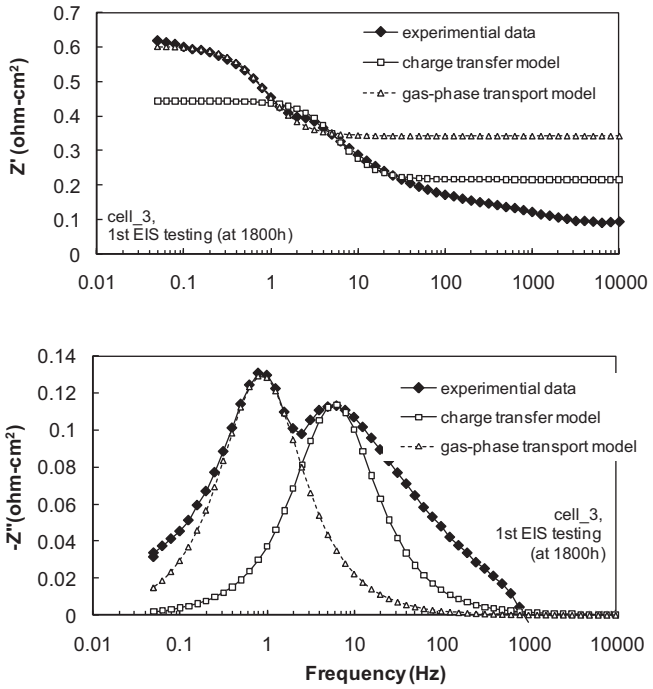

Fig. 3. Bode plots of a cell measured during the constant-current durability test of the HT-PEMFC stack. The graphical methods used in estimating each resistance are plotted over the experimental data. During the testing the stack is maintained at 0.2 A cm^{-2} and 150 °C by supplying dry hydrogen ($U_{\text{H2}} = 0.8$) and dry air ($U_{\text{O2}} = 0.5$) at near-ambient pressure, and the 10 mV voltage perturbation is applied sweeping the frequency from 10 kHz to 0.05 Hz with 10 points per decade interval.

where i is the current density applied; i_0 is the exchange current density of the oxygen reduction reaction defined when the concentration of O_2 at the catalyst site is C^*_{O2}; A_{pt} is the active surface area of the catalyst; C_{O2} is the average concentration of oxygen at the catalyst sites; α is the transfer coefficient for the oxygen reduction reaction; F is the Faraday constant; R is the gas constant; T is the temperature of the cell; and η_{ORR} is the over-potential of the ORR charge transfer reaction. It has been well accepted that the rate of ORR follows a first-order dependence in oxygen concentration [15,16]. Conflicting with previous works, the recent study by Neyerlin et al. [17] reported that the apparent reaction order with regard to oxygen concentration is rather close to 0.8 for a low-temperature PEMFC. Due to the fact that the transport loss of gas or proton, which is dependent on the structure of the electrode, can affect the apparent reaction order of ORR, it is still debatable as to what should be the apparent reaction order of ORR with regard to oxygen concentration [14,18]. In this study, the first-order reaction with regard to oxygen concentration is assumed, as shown in Eq. (1).

By rearranging the kinetic expression shown in Eq. (1), the charge transfer resistance, defined as $R_{\text{ORR}} = d\eta_{\text{ORR}}/di$, may be expressed as the following equation:

$$R_{\text{ORR}} = \frac{R \cdot T}{4\alpha \cdot F}\left[\frac{1}{i} - \frac{1}{i_0}\frac{\mathrm{d}i_0}{\mathrm{d}i} - \frac{1}{A_{\text{pt}}}\frac{\mathrm{d}A_{pt}}{\mathrm{d}i} - \frac{1}{C_{\text{O2}}}\frac{\mathrm{d}C_{\text{O2}}}{\mathrm{d}i}\right] \quad (2)$$

The R_{ORR} is determined by the rate of charge transfer, which is expressed as the current density applied, i, which is shown as the first term inside the parentheses on the right-hand side of Eq. (2). If the condition of the electrode and the transport rates of oxygen remain unchanged with a change in current density, then the rest of the terms in Eq. (2) become zero, enabling R_{ORR} to be determined only by the applied current densities and the temperature. This

value is called the *ideal charge transfer resistance* (R_{ORR}^{ideal}). Then, the discrepancy between the experimentally obtained R_{ORR} and the ideal charge transfer resistance should be the contributions of the other terms shown in Eq. (2).

The exchange current density, i_o, is specific to the materials of the catalyst and the electrolyte used for the cathode. Therefore, for the cells that have the same materials, the second term in the parentheses of Eq. (2) should be zero. The active surface area of the catalyst,A_{pt}, is determined by the condition of the electrode, and its value may change over time. At a given time and a given condition of the electrode, however, it is reasonable to assume that A_{pt} remains unchanged by changing the current density for EIS measurements, thus making the third term on the right-hand side of Eq. (2) be zero. Since the transport rate of oxygen from bulk to the reaction surface is finite, the surface concentration of oxygen,C_{O2}, depends on the consumption rate of oxygen, which is determined by the applied current density, *i*. Thus, the last term inside the parentheses on the right-hand side of Eq. (2) should be finite to cause an additional contribution to the apparent charge transfer resistance of the cathode, R_{ORR}, and the discrepancy of the measured R_{ORR} and R_{ORR}^{ideal} should be the contribution of the transport rate of oxygen through the transport-limiting layers in the cathode.

For the PEMFC cathode, the gas-phase oxygen distributed over the channels of bipolar plates diffuses through the GDL and the gas pores within the electrode; then, it is dissolved in the electrolyte in the catalyst layer, diffuses through the electrolyte film to reach the reaction sites, and is consumed. Since the permeability of oxygen through the electrolytes is relatively lower than its value in the gas phase, the limiting process of oxygen diffusion is more likely to take place through the electrolyte phase, and its contribution should be apparent at the measured R_{ORR}. Fuel cell electrodes have a porous electrode structure; the active reaction sites are distributed over the thickness of the electrode and are often represented as a transmission-line equivalent-circuit model, where a series of reaction sites are connected, as depicted in Fig. 4 [19–23]. Understanding the detailed behavior of the electrode requires an understanding of the pore structures and the various properties within the electrode. Instead, in this study, a lumped equivalent-circuit model parallels the connection of a faradaic charge transfer resistance, and a double-layer capacitance for the cathode catalyst layer is adopted to analyze the EIS data and to identify the lumped properties of the electrode that are related to the charge transfer reaction of the cathode [21,24]. As shown in Fig. 2, the diameter of the semi-circle is extracted as the representation of the effective charge transfer resistance of the cathode electrode (R_{ORR}). The value of the double-layer capacitance of the cathode catalyst layer (C_{dl}) is estimated by fitting the frequency peak value of both the imaginary and real impedances as depicted in Fig. 3. The value of the capacitance should provide the information related to the wetted surface area of both catalysts and support materials in the catalyst layer.

It has been reported by many groups that the proton transport resistance in the catalyst layer causes the 45-degree straight line at the high-frequency region of the first arc, which is observed in Fig. 2 [19,22–27]. Once the contribution of the ohmic resistance is corrected from the raw data, then the 45-degree straight line near the origin of the high-frequency arc is more clearly apparent than the one shown in Fig. 2. Depending on the degree of extension of the 45-degree line, the semi-circle shape is pushed away from the origin that is proportional to the magnitude of the proton transport resistance of the catalyst layer. Makharia et al. [24] reported that the value of the proton transport resistance (R_{H+}) taken from the graphical analysis shown in Fig. 2 follows the ohm's law in an estimation of the DC polarization loss of voltage, whereas the sum of all the proton transport resistances estimated from the transmission-line structured porous electrode ($\sum_{n=1}^{N} R_{H+}^{n}$) is approximated as thrice the value of R_{H+}. Based on their analysis, the distance of the real axis between the lower value of the fitted charge transfer semi-circle and the value of the experimentally obtained high-frequency intercept is taken as the proton transport resistance of the cathode electrode (R_{H+}), as described in Fig. 2.

In all the cases investigated, the second arc also appears at lower frequencies, as depicted in Fig. 2. This is reported by Springer et al. [19], who state that the arc at lower frequencies grows with increasing gas-phase diffusion resistance by eventually affecting the oxygen partial pressure at the electrolyte surface, thereby lowering the concentration of oxygen at the catalyst surface. In their analysis, a flooded electrode structure, where gas-phase diffusion within the active catalyst layer is not considered, is adopted, and it is demonstrated that the change in the second arc is caused by the changes in gas-phase diffusion through the GDL. In their modeling study, Guo and White [27] also reported that the presence of the concentration gradient in the gas pores that can be observed through the depth of flooded electrodes produces an additional arc at lower frequencies that are similar to the one shown in Fig. 2. To support the results discussed by Springer et al. and Guo and White, another stack, which has the same configuration as the stack tested and depicted in Fig. 1, is built and tested at two different conditions: (1) the air is fed to the cathode at $U_{O2} = 0.5$; and (2) the helox, a gas mixture of helium and oxygen,

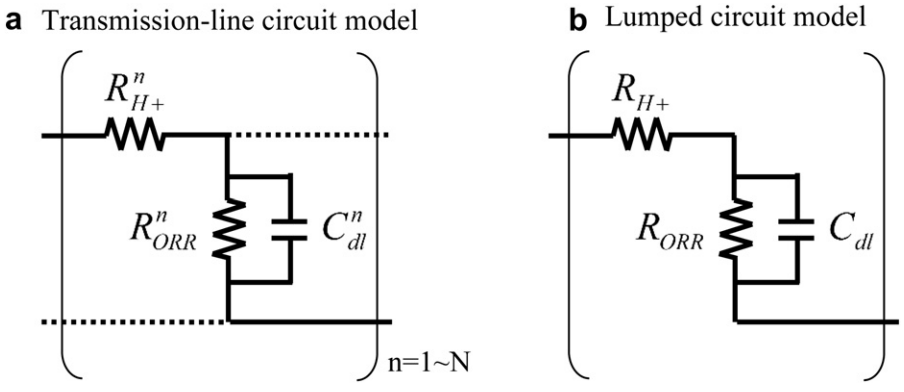

Fig. 4. One-dimensional equivalent circuit models for the cathode catalyst layer. (a) The transmission-line circuit model considers the *N* number of the catalyst sites connected in a series, including proton transport resistance through electrolyte layers and the faradaic charge transfer resistances and the double-layer capacitances at the active catalyst sites. (b) The lumped equivalent-circuit model considers a lump-summed proton transport resistance, a lump-summed charge transfer resistance, and a lump-summed double-layer capacitance in the cathode catalyst layer. In both cases, electron transport resistance is not considered.

has the same partial pressure of oxygen, is fed to the cathode at the same flow rate. When helox is used as the cathode gas, about four times faster gas-phase diffusion rate is expected while the partial pressure of O_2 remains unchanged meaning that the dissolved oxygen diffusion rate through the electrolyte phase in the catalyst layer remains the same, as in the case of the air cathode [28]. A typical result comparing the EIS responses of the air cathode and the helox cathode is shown in Fig. 5. As expected, the size of the second arc at lower frequencies is reduced in the case of helox, whereas the first arcs at higher frequencies are nearly identical. This supports the fact that at least up to the current density investigated in this study, 0.2 A cm^{-2}, the sensitivity of the rate of the gas-phase diffusion of O_2 on the apparent size of the higher-frequency arc is insignificant that the change in the gas-phase diffusion coefficient is only showed in the lower-frequency arc. Based on the supported results just mentioned, it is assumed that the magnitude of the lower-frequency semicircle is proportional to the contribution of the gas-phase transport rate through the gaseous pores in both the catalyst layer and the GDL, and the diameter of the lower-frequency semicircle is taken as the representation of the gas-phase transport resistance (R_{gt}) of the cathode, as described in Fig. 2. A delicate experimental work done by Schneider et al. [29] provides a strong evidence that, due to the ac current, the oxygen concentration oscillation excited at the air cathode in the impedance measurement may also contribute to the formation of the lower-frequency arc depending on air flow rates. This suggests that the accurate analysis of the lower-frequency semicircle requires detailed consideration of the change of oxygen concentrations along the direction of the cathode flow stream. In this study, since the changes in the lower-frequency semicircle over the period of the durability testing are monitored as the indication of the relative change of the gas transport resistance, the contribution of local-oxygen-concentration oscillation induced by the ac current is ignored.

When the condition of the cell changes while increasing the gas-phase transport resistance, its effects may result in lowering the concentration of O_2 at the catalyst surface, C_{O2}. Then, the cell performance, as described in Eq. (1), becomes lower. In addition, as expressed in Eq. (2), its effect may appear on the R_{ORR}, if the gas-phase transport rate is the limiting process or, at least, its magnitude is considerable enough to affect the overall transport rate of the oxygen. In the case where the rate of oxygen transport is limited by the transport through the electrolyte phase in the electrode, the signatures of the change of gas-phase transport rate may not appear on the R_{ORR}, because its change may not affect the overall rate of oxygen transport to the reaction sites. In any case, its effect may appear on the second arc that is shown at a lower-frequency region in Figs. 2 and 5.

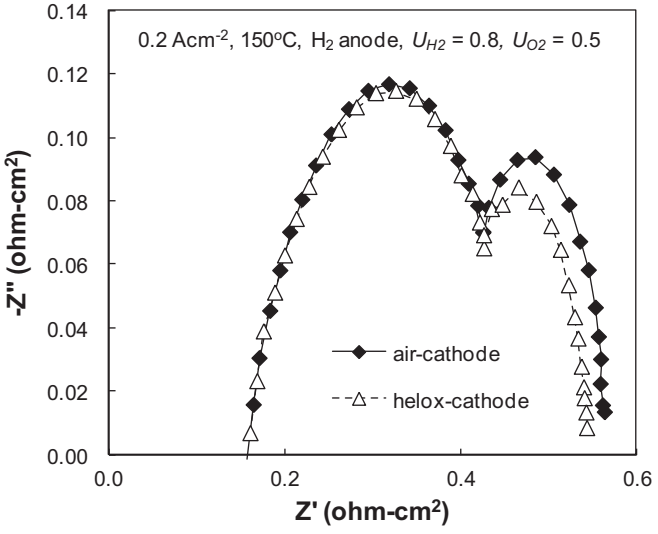

Fig. 5. Comparison of the EIS response for the air-feeding cathode versus the helox feeding cathode of a cell tested in a six-cell stack. The identical partial pressure and flow rate of oxygen are applied for both the cases supplying dry hydrogen ($U_{H2} = 0.8$) and dry air ($U_{O2} = 0.5$) at near-ambient pressure. During the testing, the stack is maintained at 0.2 A cm^{-2} and 150 °C while applying 10 mV voltage perturbation, sweeping the frequency from 10 kHz to 0.05 Hz with 10 points per decade interval.

A simplified graphical analysis methodology of EIS data is introduced based on a lumped equivalent-circuit model of the cathode depicted in Fig. 4(b). This method makes it possible to take the quantitative parameters related to the critical processes affecting the cell performance from EIS data without going through cumbersome calculations and assumptions of the detailed properties of the cell that are typically unknown. For the rest of this article, this methodology is implemented for the diagnosis of the degradation mechanisms of the individual MEA of the stack tested for long-term durability.

3.3. Investigation of degradation mechanisms

3.3.1. Ohmic resistance

Adopting the simple data analysis method described in the previous section, an attempt is made at identifying the decay mechanisms of the individual cells shown in Fig. 1. The characteristic parameters are extracted, and their values at four different runtimes are listed in Table 1. During the period of performance degradation, the ohmic resistances listed in the table show no noticeable trend over the runtime for all the MEAs. For a given MEA the values of ohmic resistance (R_{ohmic}) deviate within 0.04 Ω-cm^2 on an average, which correspond to less than an 8 mV variation of the cell voltage at 0.2 A cm^{-2}. Considering that the total voltage loss between the first and the last EIS tests varies from 28 to 69 mV depending on the MEA, the contribution of the ohmic resistance to the voltage loss during the durability test is relatively insignificant indicating that the change in the proton transport through the membrane and the electron transport through the solid conducting layers are not the main cause of the performance decay of the stack.

3.3.2. Proton transport resistance in cathode

Using the ohmic resistance identified for the individual measurements, the cathode potential (V_m^c) can be calculated by adding the voltage loss due to the ohmic resistance to the cell voltage (V_{cell}). Here, it is assumed that the anode voltage loss is insignificant to be considered. Then, the voltage loss caused by the cathode (ΔV^c) can be identified by taking the difference between the open-circuit voltage of the cathode ($V_{oc}^c = 1.1103$ V at 150 °C) and the cathode potential, as shown in Eq. (3):

$$\Delta V^c = V_{oc}^c - V_m^c = V_{oc}^c - (V_{cell} + i \cdot R_{ohmic}) \quad (3)$$

As depicted in Fig. 6, the changes of ΔV^c for individual MEAs are plotted with regard to the R_{H+} obtained from the EIS analysis, and a linear trend of increasing ΔV^c as increasing R_{H+} is observed for all the MEAs tested. This means that the proton conduction in the cathode is getting more difficult to become responsible for lowering the cathode performance observed during the period of durability testing. Since liquid-phase electrolytes, which are mobile between the membrane and the electrodes and also within the gas diffusion electrodes, are used for the MEAs, the change in the proton transport resistance may be associated with the change in the electrolyte distribution in the catalyst layer. As shown in Table 1, the amount of electrolyte in the cathode catalyst layer, as indicated by the value of the cathode double-layer capacitance, is decreased

Table 1
Parameters estimated from EIS measurements of the individual cells during the constant-current durability tested at 0.2 A cm^{-2} with dry H_2 ($U_{H2} = 0.8$) and dry air ($U_{O2} = 0.5$).

EIS testing (test hour)	Cell ID	Cell voltage, V_{cell} (V)	Ohmic resistance R_{ohmic} (ohm-cm^2)	Cathode H^+ transport resistance, R_{H+} (ohm-cm^2)	ORR charge transfer resistance, R_{ORR} (ohm-cm^2)	Cathode double-layer capacitance, C_{dl} (F-cm^{-2})	Cathode gas-diffusion resistance R_{gt} (ohm-cm^2)
1st EIS (1800 h)	1	0.6537	0.131	0.204	0.252	0.050	0.199
	2	0.6757	0.107	0.156	0.234	0.096	0.218
	3	0.6856	0.122	0.096	0.228	0.117	0.259
	4	0.652	0.163	0.198	0.250	0.038	0.170
	5	0.6807	0.108	0.050	0.246	0.100	0.248
	6	0.6725	0.120	0.055	0.264	0.092	0.300
2nd EIS (2200 h)	1	0.6372	0.094	0.324	0.264	0.030	0.190
	2	0.6686	0.098	0.204	0.228	0.070	0.212
	3	0.681	0.129	0.108	0.222	0.133	0.266
	4	0.6323	0.158	0.312	0.288	0.022	0.168
	5	0.6783	0.093	0.082	0.240	0.108	0.250
	6	0.6697	0.072	0.131	0.257	0.092	0.299
3rd EIS (2800 h)	1	0.5995	0.120	0.420	0.336	0.013	0.186
	2	0.6399	0.115	0.288	0.258	0.033	0.212
	3	0.6608	0.120	0.174	0.222	0.083	0.284
	4	0.5858	0.132	0.492	0.420	0.008	0.164
	5	0.6644	0.120	0.108	0.232	0.130	0.260
	6	0.6566	0.120	0.132	0.252	0.075	0.310
4th EIS (3300 h)	1	0.588	0.150	0.432	0.348	0.014	0.199
	2	0.6258	0.140	0.312	0.276	0.033	0.223
	3	0.6476	0.134	0.192	0.238	0.075	0.300
	4	0.5827	0.180	0.492	0.444	0.008	0.170
	5	0.6509	0.108	0.152	0.246	0.083	0.270
	6	0.6449	0.108	0.168	0.270	0.083	0.324

with runtime. Thus, it is more likely that the specific resistivity and/or the effective travel path of the proton through the electrolytes in the catalyst layer has increased, causing the increase of R_{H+} during voltage decaying. Since a lumped equivalent-circuit model shown in Fig. 4(b) is considered for the cathode electrode, the voltage loss of the cathode can be expressed as given next:

$$\Delta V^c = \eta_{ORR} + i \cdot R_{H+} \quad (4)$$

For all the MEAs, the slope of the data depicted in Fig. 6 is close to the value of the applied current density, 0.2 A cm^{-2}, which is the expected value from the relationship shown in Eq. (4). By applying Eq. (4) to each set of data shown in Fig. 6, the charge transfer over-potential for the ORR (η_{ORR}) for each point can be obtained by taking the value of the intercept of Fig. 6. Fig. 7 depicts the breakdowns of the contribution of R_{H+} and η_{ORR} that are relative to the cathode potential obtained at 1800 h for every cell. The cathode potential decays over time, whereas the contribution of the proton transport resistance of the cathode increases for all the cells responsible for the most part of the performance decay. After 2200 h, other contributions that are related to the change of the ORR charge transfer resistance appear to lower the cathode potential. Compared with the contribution of R_{H+}, however, their contribution is relatively insignificant (less than 17 mV). Fig. 7 clearly illustrates that the main cause of the performance loss during the second decay period is the increase in the effective proton transport resistance of the cathode.

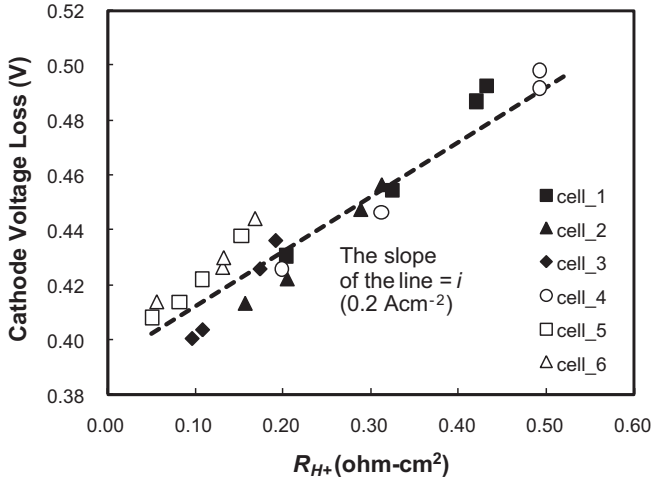

Fig. 6. Effect of the proton transport resistance on the cathode potential loss of individual cells taken at 1800, 2200, 2800, and 3300 h during constant-current durability testing of a six-cell stack. The slope of the dotted line is the expected cathode potential loss due to the change of the proton transport resistance of the cathode. During the durability test, the stack is maintained at 0.2 A cm^{-2} and 150 °C while supplying dry hydrogen ($U_{H2} = 0.8$) and dry air ($U_{O2} = 0.5$) at near-ambient pressure.

To understand the cause of the increase of R_{H+}, the relative amount of electrolytes within the electrode is estimated by comparing the double-layer capacitance obtained from the EIS analysis that is listed in Table 1. Fig. 8 shows the change in the capacitance that is related to the changes in R_{H+}. Increasing the proton transport resistance of the cathode, the apparent double-layer capacitance, which indicates the wetted surface area of both catalysts and the carbon supports in the cathode, decreases significantly, indicating that the amount of electrolyte in the cathode electrode decreases over time, causing the voltage of the cathode to be low. Assuming that the catalyst and the carbon supports are well mixed in the catalyst layer and the electrolytes are evenly distributed over the surface of carbon supports and platinum catalysts, it is reasonable to assume that the double-layer capacitance (C_{dl}) of the cathode is proportional to the active area of the catalyst (A_{pt}) as shown in the equation given next:

$$A_{pt} = \beta \cdot C_{dl} \quad (5)$$

where β is introduced as the proportional coefficient of the active platinum surface area relative to the total surface area covered by the electrolytes. By applying Eq. (5) in Eq. (1), the change in the double-layer capacitance can be correlated to the change in the cell performance. The total lumped over-potential, η_{ORR}, shown in Eq. (1) is an average potential drop between the metal potential

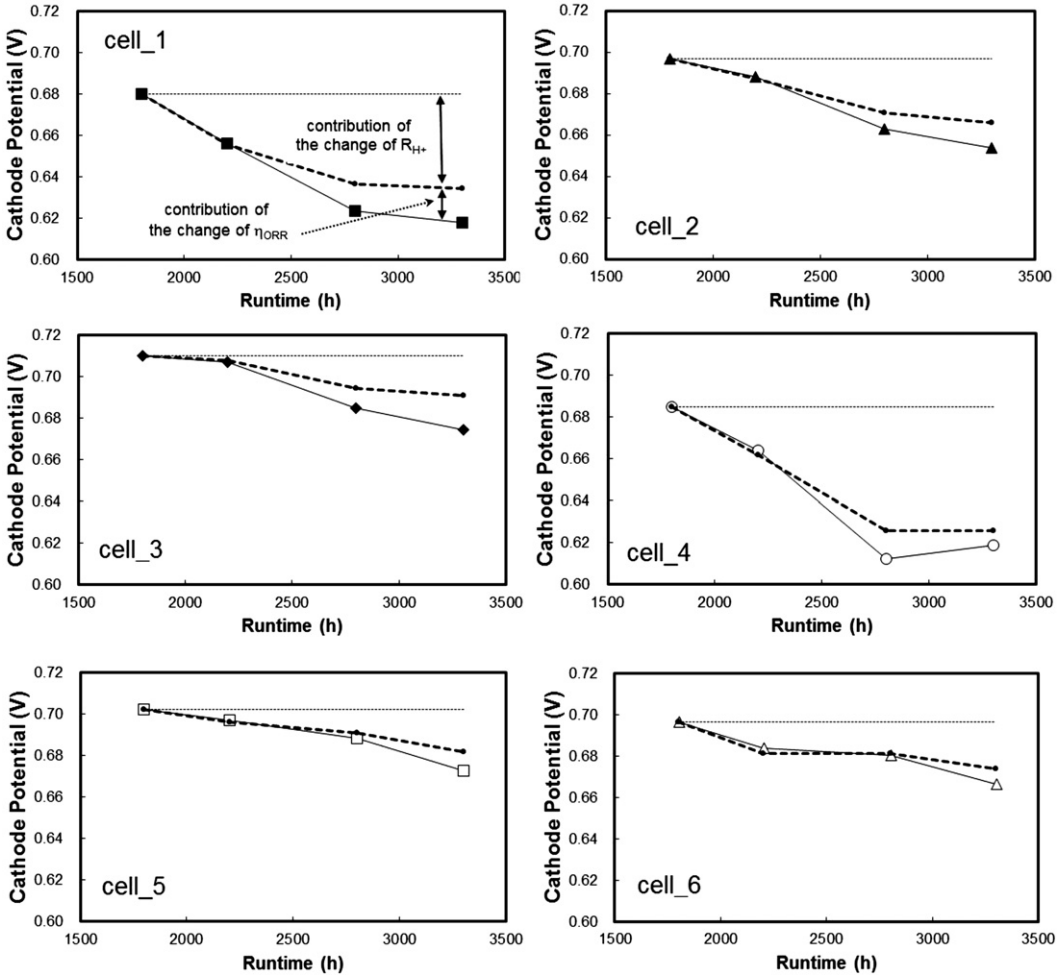

Fig. 7. Contribution of the proton transport resistance of the cathode and the ORR charge transfer resistance to the change in the cathode potential of individual cells during the constant-current durability test of a six-cell stack. The stack is maintained at 0.2 A cm^{-2} and 150 °C while supplying dry hydrogen (U_{H2} = 0.8) and dry air (U_{O2} = 0.5) at near-ambient pressure.

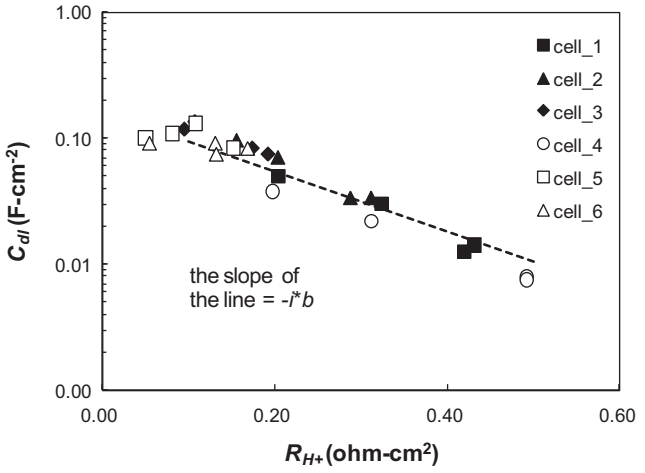

Fig. 8. Effect of the proton transport resistance of the cathode on the cathode double-layer capacitance of individual cells taken at 1800, 2200, 2800, and 3300 h during the constant-current durability test of a six-cell stack. The slope of the line is the expected change of the proton-transport resistance when the loss of the performance is caused by the loss of acid in the cathode. During the durability test, the stack is maintained at 0.2 A cm^{-2} and 150 °C while supplying dry hydrogen (U_{H2} = 0.8) and dry air (U_{O2} = 0.5) at near-ambient pressure.

(V_m^c) and the electrolyte potential (ϕ_{H+}^e) at the lumped average location in the cathode catalyst layer. Since the electrolyte potential at the reaction sites (ϕ_{H+}^e) is lowered due to the proton transport resistance of the cathode (R_{H+}), the lumped over-potential of the cell can be expressed as given next:

$$\eta_{ORR} = V_{ocv}^c - \left(V_m^c - \phi_{H+}^e\right) = V_{ocv}^c - \left(V_m^c - \left(\phi_{H+}^{m-e} + i \cdot R_{H+}\right)\right) \quad (6)$$

where ϕ_{H+}^{m-e} is the electrolyte potential at the interface between the membrane and the cathode catalyst layer. By combining Eq. (5) and Eq. (6) in Eq. (1), the following relation between the cathode proton transport resistance and the double-layer capacitance of the cathode can be obtained:

$$\ln(C_{dl}) = a - i \cdot b \cdot R_{H+} \quad (8)$$

where

$$a = \ln(i) - \ln\left(\frac{i_0 \cdot \beta \cdot C_{O2}}{C_{O2}^*}\right) - b \cdot \left(V_{ocv}^c - V_m^c + \phi_{H+}^{m-e}\right) \quad (9)$$

$$b = \frac{4 \cdot \alpha \cdot F}{R \cdot T} \quad (10)$$

Assuming that the η_{ORR} is mainly affected by the sluggish transport of the proton through the cathode catalyst layer to the active sites, the expected change in the double-layer capacitance can be estimated by Eq. (8). As depicted in Fig. 8 the change in the double-layer capacitance follows the expected slope of $-i^*b$. The value of b, which is called the *Tafel slope*, is calculated at 150 °C assuming the reported transfer coefficient of the oxygen reduction reaction, $\alpha = 0.25$ [17]. The loss of acid in the catalyst layer can make the conduction of the proton to the active catalyst sites more difficult by increasing the proton transport resistance in the catalyst layer. If the increase in the proton transport resistance is the main cause behind of lowering the cathode potential, as supported by Fig. 7, then the voltage loss of the cathode should follow the expected trend with the slope of $-i^*b$, as shown in Eq. (8). The trend depicted in Fig. 8 supports the hypothesis that the loss of cathode potential due to the increase in the proton transport resistance may be caused by the acid loss in the cathode. One thing to be noticed is that the cells maintained a relatively higher amount of the electrolyte (cell_3, cell_5, and cell_6) show a relatively poor correlation compared with the other cells. This is probably the reason that the remaining electrolyte in the catalyst layer is still high enough; therefore, the change in the proton transport resistance may not be linearly proportional to the loss of the wetted active surface area. Nonetheless, it can be concluded that the loss of electrolyte in the cathode is the main cause of increasing the proton transport resistance in the catalyst layer.

To confirm the loss of acid during the durability test, the stack is disassembled after a 4000-h operation, and the acid-base titration is performed, which determines the amount of phosphoric acid changed during the test. As shown in Fig. 9, a significant amount of phosphoric acid is removed from the MEAs after 4000 h of continuous operation. Among the MEA components, a relative percentage of the acid removed is the most significant for the cathode GDE, showing only 32.7 ± 8.5 wt% remaining, whereas the remaining percentage of acid in the membrane and the anode GDE show 64.6 ± 5.7 wt% and 41.7 + 11.6 wt%, respectively. From the value of double-layer capacitance estimated by the EIS analysis, it is estimated that the amount of acid remaining in the cathode catalyst layer at 3300 h can be as low as 20 wt% of the amount at 1800 h. Interestingly, the amount of acid in the cathode GDE including the catalyst layer and the GDL from the titration, gives a minimum of 20 wt% remaining at the end of the 4000 h of testing. When assuming that most of the acid is removed during the second decay period, the magnitude of acid loss estimated by the EIS analysis is within a reasonable range observed by the titration. However, between the MEAs, there is no specific trend related to the amount of acid remaining, and no correlation to the final performance of the MEAs depicted in Fig. 1 is observed. This is probably due to the fact that less than 4 wt% of the volume is taken for sampling, so that the remaining amount of acid of each piece of MEA is not represented accurately enough to be compared among the MEAs. Since the heating is done using cartridges inserted into the endplates, a non-uniform distribution of temperature among and within the cells are unavoidable and may be another factor that affects the final distribution of acid remaining among and within MEAs. In addition, during the shut-down procedures, the electrolyte may be redistributed within the MEA components, thus becoming another source of inaccuracy to estimate the amount of acid distribution within a MEA. In general, the acid-base titration results support the fact that, during the durability testing, a significant amount of electrolyte is removed from the cathode electrodes, as indicated by the EIS analysis.

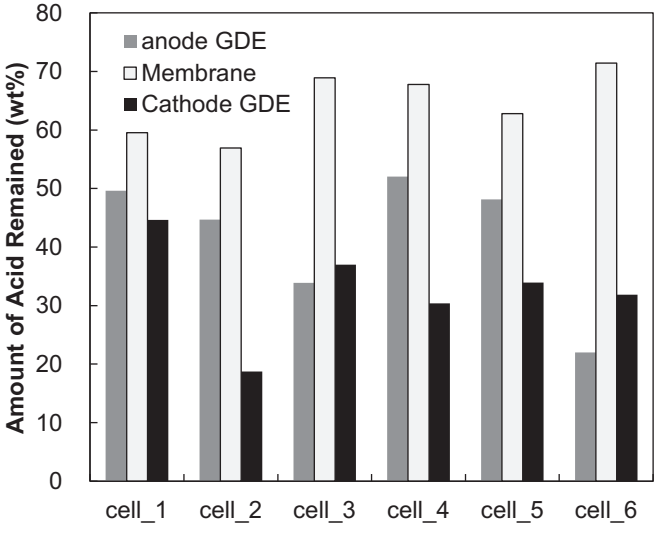

Fig. 9. The amount of phosphoric acid remaining in the MEAs after a 4000-h durability test of the six-cell stack. The initial amount and the amount remaining in anode GDE, membrane, and cathode GDE are measured by taking five pieces of 1-cm diameter samples from each component. During the durability testing, the stack is maintained at 0.2 A cm^{-2} and 150 °C while supplying dry hydrogen ($U_{H2} = 0.8$) and dry air ($U_{O2} = 0.5$) at near-ambient pressure.

3.3.3. Charge transfer resistance of the cathode

From the analysis just discussed, it is demonstrated that the main cause of the performance decay between 1800 h and 3300 h is the loss of acid in the cathode electrode, which is effective in increasing the proton transport resistance in the cathode. Once the contribution of the proton transport resistance in the cathode is quantified and corrected from the cathode potential, then the apparent contribution of the charge transfer loss of the cathode reaction, η_{ORR}, can be obtained as discussed in the previous section. As depicted in Fig. 7, the contribution of η_{ORR} becomes higher with runtime. In this section, an attempt is made at identifying the mechanism behind the increase in ORR charge transfer loss using the experimental signatures obtained from the EIS analysis.

By rearranging Eq. (1), the potential sources of the increase in the cathode charge transfer loss can be expressed as follows:

$$\eta_{ORR} = \frac{1}{b}\left[\ln(i) - \ln\left(\frac{i_0}{C^*_{O2}}\right) - \ln(A_{pt}) - \ln(C_{O2})\right] \quad (11)$$

The voltage loss of the cathode charge transfer reaction is determined by the applied current density, as shown in the first term on the right-hand side of the equation, and also by the inherent charge transfer rate, which is determined by the materials of the catalyst and the electrolyte at a given temperature, pressure and concentration of oxygen at the surface, C^*_{O2}, as shown in the second term of Eq. (11). For a given MEA, when an operating condition is set, then the first and the second terms should remain unchanged over time. During the durability test, however, the distribution of electrolytes and the conditions of the electrode may be changed, causing the active surface area of the catalyst (A_{pt}) and/or the concentration of oxygen at the reaction site (C_{O2}), which are described as the third and the last term of Eq. (11), to be changed. With the loss of acid in the catalyst layer as discussed in the previous section, A_{pt} may be changed. In the case of cell_1, cell_2, and cell_4, the acid loss in the cathode is significantly high such that the change in the cathode potential is dominated by the voltage loss due to the increase in the proton transport resistance of the cathode, as depicted in Fig. 8. In the case of cell_3, cell_5, and cell_6, the change in R_{H+} is less significant such that its correlation to the double-layer capacitance is less apparent, probably because

the other source of polarization, R_{ORR}, may be relatively significant as well. To find a correlation between η_{ORR} and A_{pt}, Eq. (5) is combined to Eq. (1); then, the following correlation can be obtained:

$$\ln(C_{dl}) = a' - \frac{1}{b}\cdot\eta_{ORR} \tag{12}$$

where

$$a' = \ln(i) - \ln\left(\frac{i_0\cdot\beta\cdot C_{O2}}{C^*_{O2}}\right) \tag{13}$$

Fig. 10 depicts the correlation between C_{dl} obtained from the EIS analysis and η_{ORR} obtained from the voltage of cell_3, cell_5, and cell_6, and it shows that the magnitude of the ORR charge transfer loss of the cells correlated well with the observed trend of the double capacitance following the expected slope described in Eq. (12). This indicates that the source of the increase of η_{ORR} of cell_3, cell_5, and cell_6 may be due to the decrease in the active surface area as shown in the third term on the right-hand side of Eq. (11).

Another possible source of increasing η_{ORR} is the change in the oxygen concentration at the reaction sites, as described in the last term of Eq. (11). As discussed earlier in the discussion section, the contribution of the oxygen transport resistance should be apparent in the ORR charge transfer resistance, R_{ORR}, obtained from the EIS data, and its relation to the η_{ORR} obtained from the cell voltage is depicted in Fig. 11. In the case of cell_3, cell_5, and cell_6, the values of R_{ORR} are not changed while increasing the voltage loss for the charge transfer reaction. This means that the resistance of oxygen transport to the reaction site, as shown in the last term of Eq. (2), is unchanged with the runtime for cell_3, cell_5, and cell_6. In contrast, the values representing the gas-phase oxygen transport resistance, R_{gt}, have increased for cell_3, cell_5 and cell_6 by increasing η_{ORR} (see Fig. 12). This specifies that the gas-transport rate through the gas pores of GDE and/or in the catalyst layer has increased while η_{ORR} increases. Nonetheless, the transport-limiting step is carried out through electrolyte films in the catalyst layer; therefore the overall oxygen transport rate to the catalyst site does not change during this period, as indicated by Fig. 11. Depending on the relative magnitude of the gas-phase diffusion velocities compared with the limiting transport rate through the electrolyte, the concentration of oxygen at the reaction sites may or may not be changed to increase η_{ORR}. There is no further evidence whether the lower gas-diffusion velocity decreases the concentration of O_2 at the reaction sites and lowers the η_{ORR} or not. The contribution of the changes in the active catalyst area, however, is correlated well with the change of the ORR charge transfer loss of the cells (see Fig. 10), it is more likely that the contribution of gas transport resistance on the concentration of oxygen at the reaction sites are relatively insignificant to increase the charge transfer loss of the cathodes. In summary, in the case of cell_3, cell_5, and cell_6, it appears that some of the acid (less than 35%) has moved away from

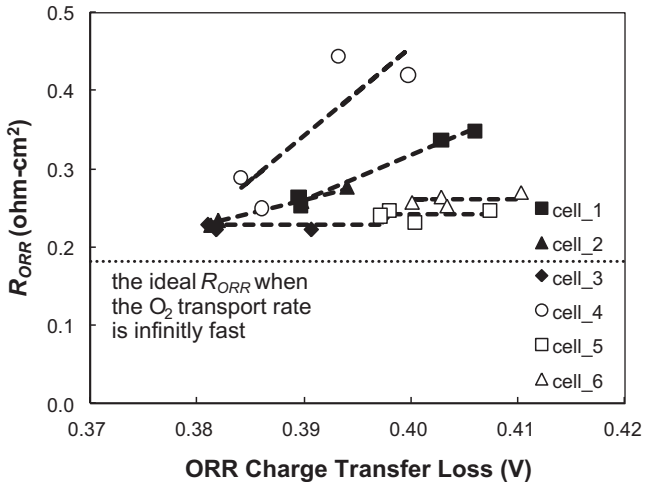

Fig. 11. Effect of the charge transfer loss of the cathode estimated from the measured cell voltage on the ORR charge transfer resistance measured from the EIS measurements taken at 1800, 2200, 2800, and 3300 h during the constant-current durability test of a six-cell stack. The lines for all the cells are the liner trend line of the data. The dotted flat line at the bottom represents the value of the ideal ORR charge transfer resistance when the oxygen transport rate is infinitely fast such that the resistance is determined by the current density applied and the ideal Tafel slope. During the durability test, the stack is maintained at 0.2 A cm^{-2} and 150 °C while supplying dry hydrogen ($U_{H2} = 0.8$) and dry air ($U_{O2} = 0.5$) at near-ambient pressure.

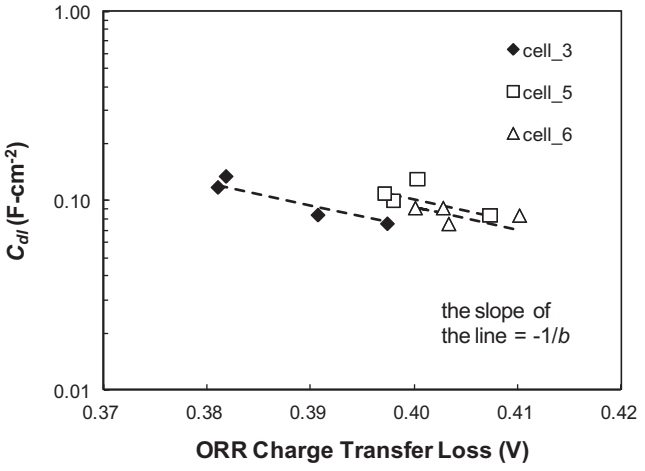

Fig. 10. Effect of the ORR charge transfer loss of cathode on the cathode double-layer capacitance of cell_3, cell_5, and cell_6 taken at 1800, 2200, 2800, and 3300 h during the constant-current durability test of a six-cell stack. The slope of the line is the expected change in the double-layer capacitance when the loss of the ORR charge transfer reaction is caused by the change in the active catalyst area, which is linearly proportional to the change in the double-layer capacitance of the cathode. During the durability test, the stack is maintained at 0.2 A cm^{-2} and 150 °C while supplying dry hydrogen ($U_{H2} = 0.8$) and dry air ($U_{O2} = 0.5$) at near-ambient pressure.

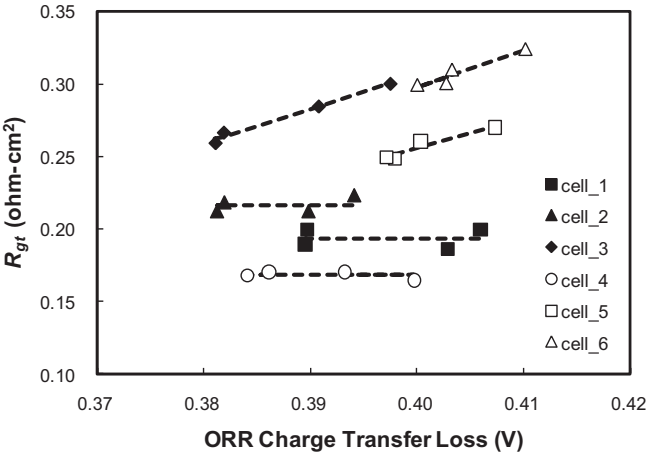

Fig. 12. Effect of the charge transfer loss of the cathode estimated from the measured cell voltage on the gas-phase oxygen transport resistance measured from the EIS measurements taken at 1800, 2200, 2800, and 3300 h during the constant-current durability test of a six-cell stack. The lines for all the cells are the liner trend line of the data. During the durability test, the stack is maintained at 0.2 A cm^{-2} and 150 °C while supplying dry hydrogen ($U_{H2} = 0.8$) and dry air ($U_{O2} = 0.5$) at near-ambient pressure.

the active catalyst sites which the active surface area has decreased (see Fig. 10). At the same time, the acid removed from the active catalyst sites resides within the gas-diffusion path in the GDE and blocks some of the gas-diffusion paths (see Fig. 12) to lower the rate of gas-phase oxygen diffusion, even though the overall rate of oxygen transport remains unchanged (see Fig. 11) during the operation as depicted in Fig. 11. This indicates that the transport limiting step of oxygen is through the electrolytes in the cathode catalyst layer.

In the case of cell_1, cell_2, and cell_4, the amount of acid is already significantly lower such that it also affects the ORR charge transfer resistance to be higher, as shown in Fig. 11. As previously discussed and related to Eq. (2), the change in R_{ORR} during the constant current durability test is due to the change in the oxygen transport rate to the active catalyst sites. As depicted in Fig. 11, the value of R_{ORR}^{ideal} should be 0.182 Ω-cm^2 (at 0.2 A cm^{-2}, 150 °C) if the gas transport rates through the gas pores as well as the electrolyte films are infinitely fast. The difference of the value is proportional to the relative transport rate of the oxygen through the transport-limiting layer. The values of cell_3, cell_5 and cell_6 depicted in Fig. 11 are higher than the value of R_{ORR}^{ideal} and remain unchanged during the testing. In the case of cell_1, cell_2, and cell_4, however, the values of R_{ORR} show an increasing trend with increasing η_{ORR} (see Fig. 11). At the same time, the gas-phase transport resistances of cell_1, cell_2, and cell_4 shows no changes with increasing η_{ORR} (see Fig. 12). This indicates that the oxygen transport rate of cell_1, cell_2, and cell_4 is limited through electrolytes in the cathode catalyst layer, and the rate of the oxygen transport through the electrolytes decreases with increasing the ORR charge transfer voltage loss. Since the difference between the values of theR_{ORR} and the R_{ORR}^{ideal} gives the relative rate of oxygen transport through the transport-limiting layer, in this case, the transport rate through the electrolyte phase, the oxygen transport rate can be derived from Eq. (2) and expressed as given next:

$$R_{ORR} - R_{ORR}^{ideal} = -\frac{1}{b}\cdot\frac{1}{C_{O2}}\cdot\frac{dC_{O2}}{di} \tag{14}$$

From the total flux of oxygen reached at the catalyst sites that is determined by the current density applied, the concentration at the reaction surface can be described as given next:

$$C_{O2} = C_{O2}^{g-e} - \frac{i}{4F}\frac{\Delta l^e}{D_{O2}^{eff,e}} \tag{15}$$

By applying Eq. (15) in Eq. (14), R_{ORR} at a given runtime can be expressed as given next:

$$R_{ORR} = R_{ORR}^{ideal} + \frac{\dfrac{1}{4b\cdot F\cdot\left(D_{O2}^{eff,e}/\Delta l^e\right)}}{C_{O2}^{g-e} - \dfrac{1}{4b\cdot F\cdot\left(\dfrac{D_{O2}^{eff,e}}{\Delta l^e}\right)}} \tag{16}$$

where C_{O2}^{g-e} is the concentration of oxygen at the gas–electrolyte interface; Δl^e is the effective diffusion distance between the gas–electrolyte interface and the lumped average location of the catalyst site; and $D_{O2}^{eff,e}$ is the effective diffusion coefficient of oxygen in the electrolyte. By comparing the change in R_{ORR} the relative change in the diffusion rate through the electrolyte phase $(D_{O2}^{eff,e}/\Delta l^e)$ can be calculated with regard to a reference value. In this case, the value of 1800 h is taken as the reference point, and the relative change in the diffusion rate through the electrolyte phase is derived as shown next:

$$\left(\frac{D_{O2}^{eff,e}}{\Delta l^e}\right) = A\cdot\left(\frac{D_{O2}^{eff,e}}{\Delta l^e}\right)^{t=1800h} \tag{17}$$

where

$$A = \left(\frac{i\cdot b + \dfrac{1}{R_{ORR} - R_{ORR}^{ideal}}}{i\cdot b + \dfrac{1}{R_{ORR}^{t=1800h} - R_{ORR}^{ideal}}}\right) \tag{18}$$

Therefore, at a given runtime, the relative change in the diffusion rate through the electrolytes of cell_1, cell_2, and cell_4 is estimated by applying the value of R_{ORR} obtained from the EIS analysis in Eq. (18). As depicted in Fig. 13, the diffusion rate through the electrolyte phase decreases with time, proving to be between 45 and 65% of the values at 1800 h. The decrease in the diffusion rate, either/both by decreasing the effective diffusion coefficient with the loss of acid in the catalyst layer or/and by increasing the required diffusion path due to the loss of the number of active catalyst sites, makes the effective concentration of oxygen at the reaction sites lower, causing the η_{ORR} to be increased. In any case, since the binary diffusion coefficient of oxygen in the electrolytes remains constant, the decrease in the diffusion rate should be associated with the increase in travel distance. Since the amount of acid remaining in the cathode is significantly reduced, the number of active sites accessible to both oxygen and protons become limited such that the oxygen has to travel further; this causes the tortuosity and the required diffusion length to be increased, hence, the diffusion rate to be lower as depicted in Fig. 13. Therefore, in the case of cell_1, cell_2, and cell_4, it can be said that the increase in η_{ORR} during the second decay period is caused by the increase in the oxygen transport resistance through the electrolyte phase in the cathode catalyst layer so that the effective oxygen concentration at the catalyst site becomes lower, whereas the gas-phase diffusion resistance remains unchanged.

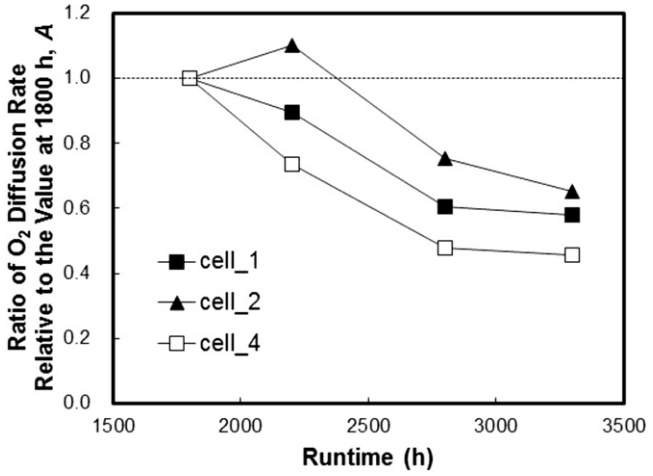

Fig. 13. Estimated changes in the oxygen diffusion velocity through the electrolytes in the cathode catalyst layer relative to the values at 1800 h of cell_1, cell_2, and cell_4 of a six-cell stack. During the durability test, the stack is maintained at 0.2 A cm^{-2} and 150 °C while supplying dry hydrogen (U_{H2} = 0.8) and dry air (U_{O2} = 0.5) at near-ambient pressure.

4. Conclusions

In this study, the degradation mechanism of an HT-PEMFC stack has been investigated using the EIS method. During the durability test, the increase in proton transport resistance and the decrease in double-layer capacitance in the cathode are observed. This suggests that the main cause of the high-rate performance degradation of the stack is the loss of phosphoric acid in the cathode electrode, lowering the protons conduction rate through the cathode catalyst layer and the cell voltage during the constant-current durability test. In addition to the increase in the proton transport resistance in the cathode, the ORR charge transfer loss is increased as well. The change of ORR charge transfer resistance is related to the change of oxygen transport rate to the active catalyst sites. For the cases investigated here it is concluded that the transport limiting step of oxygen is through the electrolytes in the catalyst layer. For the MEAs of cell_1, cell_2, and cell_4 the acid remaining during the second decay period is considerably low such that the number of active catalyst sites is already reduced causing the required oxygen transport path from the surface of electrolyte layer to the available active catalyst sites to become longer, resulting in the increase of ORR charge transfer resistance of the cells. The MEAs, which have a critical amount of acid remaining (cell_3, cell_5, and cell_6), however, show the increase in the gas-diffusion resistance of the cathode GDEs, whereas the overall oxygen transport resistance through the gas pores and the electrolytes remains unchanged. Meanwhile, it is observed that the decrease in the active catalyst surface area may be the cause of increasing the ORR charge transfer loss of the cathode.

The EIS is widely used as an *in-situ* diagnostic tool for understanding the behavior of fuel cells. The extraction of meaningful parameters related to the actual process occurring inside the cell, however, is limited, and it requires cumbersome numerical analysis by discovering the properties related to the structures of the cell. In this study, a simplified graphical method of obtaining experimental signatures about the condition of the cell using the EIS analysis is introduced, and it demonstrates that the analysis leads to the identification of the potential sources of polarization of the cell, qualitatively as well as quantitatively. This work provides a possibility that the EIS method can be a simple and useful diagnostic tool which investigates degradation mechanisms of the HT-PEMFC stacks.

References

[1] S. Srinivasan, R. Mosdale, P. Stevens, C. Yang, Ann. Rev. Energy Environ. 24 (1999) 281–328.
[2] M.F. Mathias, R. Makharia, H.A. Gasteiger, J.J. Conley, T.J. Fuller, C.J. Gittleman, S.S. Kocha, D.P. Miller, C.K. Mittelsteadt, T. Xie, S.G. Yan, P.T. Yu, Electrochem. Soc. Interface (Fall 2005) 24–27.
[3] J. Zhang, Z. Xie, J. Zhang, Y. Tang, C. Song, T. Navessin, Z. Shi, D. Song, H. Wang, D.P. Wilkinson, Z.S. Liu, S. Holdcroft, J. Power Sources 160 (2006) 872–891.
[4] H. Tang, Z. Wan, M. Pan, S.P. Jiang, Electrochem. Commun. 9 (2007) 2003–2008.
[5] E.I. Santiago, R.A. Isidoro, M.A. Dresch, B.R. Matos, M. Linardi, F.C. Fonseca, Electrochim. Acta 54 (2009) 4111–4117.
[6] J.S. Wainright, M.H. Litt, R.F. Savinell, Handbook of Fuel Cells –Fundamentals, vol. 3, Technology and Applications, 2003, 436–446.
[7] J.A. Asensio, S. Borros, P.G. Romero, J. Electrochem. Soc. 151 (2004) A304–A310.
[8] T.J. Schmidt, J. Baurmeister, J. Power Sources 176 (2008) 428–434.
[9] J.C. Wannek, B. Kohnenl, H.F. Oetjen, H. Lippert, J. Mergel, Fuel Cells 8 (2008) 87–95.
[10] Q. Li, J.O. Jensena, R.F. Savinell, N.J. Bjerrum, Prog. Polym. Sci. 34 (2009) 449–477.
[11] Q. Li, R. He, J.-A. Gao, J.O. Jensen, N.J. Bjerrum, J. Electrochem. Soc. 150 (2003) A1599–A1605.
[12] K. Kwon, J.O. Park, D.Y. Yoo, J.S. Yi, Electrochim. Acta 54 (2009) 6570–6575.
[13] S. Choi, J. Park, W. Lee, US Patent #2009/0075148.
[14] D.C. Seel, B.C. Benicewicz, L. Xiao, T.J. Schmidt, Handbook of Fuel Cells – Fundamentals, vol. 5, Technology and Applications, 2009, 300–312.
[15] K.C. Neyerlin, W. Gu, J. Jorne, H.A. Gasteiger, J. Electrochem. Soc. 153 (2006) A1955–A1963.
[16] A. Parthasarathy, S. Srinivasan, A.J. Appleby, J. Electrochem. Soc. 139 (1992) 2856–2862.
[17] A.Z. Weber, J. Newman, Chem. Rev. 104 (2004) 4679–4726.
[18] M.L. Perry, J. Newman, E.J. Cairns, J. Electrochem. Soc. 145 (1998) 5–15.
[19] T.E. Springer, T.A. Zawodzinski, M.S. Wilson, S. Gottesfeld, J. Electrochem. Soc. 143 (1996) 587–599.
[20] F. Jaouen, G. Lindbergh, J. Electrochem. Soc. 150 (2003) A1699–A1710.
[21] T.E. Springer, I.D. Raistrick, J. Electrochem. Soc. 136 (1989) 1594–1603.
[22] I.D. Raistrick, Electrochim. Acta 35 (1990) 1579–1586.
[23] M. Eikerling, A.A. Kornyshev, J. Electroanal. Chem. 475 (1999) 107–123.
[24] R. Makharia, M.F. Mathias, D.R. Baker, J. Electrochem. Soc. 152 (2005) A970–A977.
[25] M.C. Lefebvre, R.B. Martin, P.G. Pickup, Electrochem. Solid-State Lett. 2 (1999) 259–261.
[26] Q. Guo, M. Cayetano, M.Y.- Tsou, E.S. De Castro, R.E. White, J. Electrochem. Soc. 150 (2003) A1440–A1449.
[27] Q. Guo, R.E. White, J. Electrochem. Soc. 151 (2004) E133–E149.
[28] E.L. Cussler, Diffusion Mass Transfer in Fluid Systems, Cambridge University Press, New York, 1984.
[29] I.A. Schneider, S.A. Freunberger, D. Kramer, A. Wokaun, G.G. Scherer, J. Electrochem. Soc. 154 (2007) B383–B388.